Post-Print

When citing this work, cite the original published paper.

Permanent link to this version
http://hdl.handle.net/11311/1091927

ASME Accepted Manuscript Repository

Maurizio   Quadrio
_____   _____
First   *Last*

ASME Paper Title: On the Turbulence Modeling of Blood Flow in a Stenotic Vessel
_____

_____

Authors: Lui, Mattia; Martino, Savino; Salerno, Mario; Quadrio, Maurizio
_____

ASME Journal Title: Journal of Biomechanical Engineering
_____

Volume/Issue   142/1_____   Date of Publication (VOR* Online)   Oct. 1st, 2019

ASME Digital Collection URL: https://asmedigitalcollection.asme.org/biomechanical/article/doi/10.1115/1.4044029/
Turbulence-Modeling-of-Blood-Flow-in-a

DOI: 10.1115/1.4044029
_____

On the turbulence modeling of blood flow in a stenotic vessel

Mattia Lui
Dept. Aerospace Sciences and Technologies
Politecnico di Milano, Italy

Savino Martino
Dept. Aerospace Sciences and Technologies
Politecnico di Milano, Italy

Mario Salerno
Angiology Unit, IRCCS ICS Maugeri
Tradate, Italy

Maurizio Quadrio

Professor
Department of Aerospace Sciences and Technologies
Politecnico di Milano, Italy
Email: maurizio.quadrio@polimi.it

Blood flow dynamics in a stenosed, subject-specific carotid bifurcation is numerically simulated using Direct Numerical Simulation (DNS) and Reynolds-averaged Navier–Stokes (RANS) equations closed with turbulence models. DNS is meant to provide a term of comparison for the RANS calculations, which include classic two-equations models ($k-\varepsilon$ and $k-\omega$) as well as a transitional three-equations eddy-viscosity model ($k_T - k_L - \omega$). Pulsatile inlet conditions based on in-vivo ultrasound measurements of blood velocity are used. The blood is modelled as a Newtonian fluid, and the vessel walls are rigid. The main purpose of this work is to highlight the problems related to the use of classic RANS models in the numerical simulation of such flows.

The time-averaged DNS results, interpreted in view of their finite-time averaging error, are used to demonstrate the superiority of the transitional RANS model, which is found to provide results closer to DNS than those of conventional models. The transitional model shows better predictive capabilities in terms of turbulence intensity, temporal evolution of the pressure along the cardiac cycle, and the oscillatory shear index (OSI). Indeed, DNS brings to light the locally transitional or weakly turbulent state of the blood flow, which presents velocity and pressure fluctuations only in the post-stenotic region of the internal carotid artery during systole, while the flow is laminar during diastole.

1 Introduction

Atherosclerosis is a common inflammatory disease characterized by the development of lesions, or plaques, in the inner coat of arteries [1]. Atherosclerotic plaques develop and change over decades, leading to the narrowing of the artery cross-section. This phenomenon, called stenosis, changes the hemodynamic conditions within the vessel and prevents a normal blood flow. Stenoses may be dangerous when the hemodynamic conditions lead to the rupture of the plaque, or facilitate the formation of thrombi, obstructing the artery and thus precluding proper blood supply to organs.

One of the most common areas for the formation of atherosclerotic plaques is the carotid sinus, which is the part of the internal carotid artery (ICA) next to the carotid bifurcation. Since the ICA supplies blood to the brain, its obstruction may be responsible for an ischemic stroke, which is the second cause of death after coronary artery disease [2] and the leading cause of long-term disability [3], obviously affecting the health budget for a significant amount, 38.6 bil-

lion dollars in 2009 in the U.S. according to [4].

Over the years, several hemodynamic factors have been suggested to influence the formation, development and eventual rupture of atherosclerotic plaques. Regions with low wall-shear stresses (WSS) have been associated to high probability of plaque formation [5–9]. On the other hand, high and temporally oscillating WSS are related to plaque's destabilization and rupture [10–12]. Moreover, as reported by [13], [14] and [15], high WSS within the stenosis may activate platelets which, in recirculation areas downstream of the stenosis, could form thrombi and occlude the vessel. For these reasons, it is important to properly characterize the hemodynamic behavior of a stenotic vessel.

To date, the severity of a stenosis and the related need for surgical intervention are often assessed only via the percentage of occlusion of the arterial lumen, neglecting the geometrical details of the plaque. However, such details play a fundamental role as they influence the hemodynamic parameters and therefore stenoses with equal extensions might imply different degrees of danger [16]. The same authors also noted that in case of severe stenosis the pressure drop in correspondence of the vessel narrowing could lead to a collapse of the artery.

Thanks to the current advances in computational fluid dynamics (CFD), numerical simulations are nowadays considered a useful tool to investigate the characteristics of such flows, providing a level of detail which is not attainable by *in vivo* experimental techniques. The latter, such as phase-contrast magnetic resonance imaging or ultrasound, can provide velocity measurements, but suffer from low spatial resolution [17–19]. The characterization of the blood flow through stenosed vessels has been approached in various ways over the years. In the brief review that follows, our focus is only on CFD-oriented studies, which are grouped according to the complexity of the geometrical model.

1.1 Idealized geometries

Early studies employed idealized vessel geometries modified by geometrically simple narrowings [15, 20–24]. All considered a plane channel flow with a semicircular stenosis [20, 23, 24] or cosine-shaped stenosis [15, 21] on a single wall, or a semicircular stenosis on both walls [22]. The first three studies investigated the potential of large eddy simulation (LES), while the last two performed a direct numerical simulation (DNS). Both techniques solve for the three-dimensional unsteady velocity and pressure fields: the former models the small-scale turbulent motions to some extent, while the latter is a no-model, more computationally demanding approach that solves the flow down to the smallest dissipative scales relevant for the flow dynamics.

Other studies considered a cylindrical geometry, i.e. pipe flow. For example, [25, 26] performed a DNS with axisymmetric and non-axisymmetric stenosis with pulsatile inlet, and highlighted that the laminar flow at the inlet section experiences transition to turbulence when a slight asymmetry is present in the geometry of the stenosis. This study clearly revealed the complex nature of the flow, which is laminar upstream of the model stenosis, and becomes transitional and/or turbulent just downstream, with possible relaminarization further downstream the narrowing at certain phases of the cardiac cycle.

It was henceforth natural to explore the potential of transitional models in the context of the Reynolds-Averaged Navier–Stokes (RANS) equations, which are computationally less expensive than the DNS or LES approach. Transitional RANS models were assessed in [27], where various RANS and LES models were compared on the same, idealized geometry; [28] compared the performance of a transitional version of the $k-\omega$ turbulence model on the same idealized geometry introduced by [25]. All these studies suggested that, in the present context, any model capable of "seeing" the laminar-turbulent transition should be more appropriate.

1.2 Parametric idealized geometries

A further category of studies involving simplified geometries concerns simulations carried out on parametric geometries. This approach aims at reproducing the real form of the carotid bifurcation by using simple parametric shapes created by computer aided design (CAD) software. The advantage of this strategy is that the shape and degree of the stenosis can be easily modified by changing a few parameters, allowing one to investigate how they affect the flow. [29] and [30] assessed the reliability of the transitional version of the $k-\omega$ model in this situation. The first study demonstrated that the transitional model agrees better with experimental data on the same geometry when compared to the classic $k-\omega$ model. The second one lacks a comparison with DNS or experimental data, but clearly demonstrates the capability of the transitional model to predict transition to turbulence above a certain degree of stenosis.

1.3 Patient-specific geometries

A number of CFD studies were carried out on patient-specific geometries obtained with medical imaging techniques, such as magnetic resonance imaging (MRI) or computed tomography (CT). Obviously, this approach is computationally more expensive, but provides the most clinically useful information. In this context, [31] and [32] neglected both transition and turbulence, and carried out a laminar simulation using commercial software (*Fluent*, *ADINA*). In the second paper a non-Newtonian rheological model is used to account for the shear's dependence of the viscosity. [33] tried two variants of the $k-\varepsilon$ model on a 2D geometry with non-Newtonian fluid, and verified their inadequacy to represent the transitional nature of the flow. [8] used an high-Re $k-\varepsilon$ model, usually adopted for fully turbulent flows, and failed to correctly describe the transitional and laminar behavior. [34] and [35] explored the transitional RANS models (in particular the SST-transition model), suggesting that the latter might be more accurate than the classic two-equation models. Also the LES technique was investigated by [36], who compared it with the $k-\varepsilon$ model (the Chien variant) in a steady case. As expected, the LES analysis better captured the transitional

nature of the flow, at the expense of an increased computational cost. In all these studies, the validation of the fluid dynamics model, when present, is not performed on the same patient-specific geometry, but on the simpler ones mentioned before (pipe or channel flow).

Perhaps the most accurate description of the flow to date through a patient-specific stenosed carotid bifurcation was provided by [37], who performed a DNS on a geometry reconstructed by MRI. They used a pulsatile, fully developed inlet boundary condition, with blood considered as a Newtonian fluid and the vessel considered as a rigid wall. The authors used a spectral-element solver, with no turbulence modelling, on a mesh with approximately $1,854,000$ grid points and a time step of $\Delta t = 10^{-5} s$, such that all the scales of motion are resolved. Even if this approach is the only one that provides an accurate description of the flow, its computational cost is large (in this case, each simulated cardiac cycle took 20 hours using 256 computing processors), and thus DNS is not a suitable method to produce clinically relevant information within a short time.

1.4 Goal of the present work

From the summary presented above, it emerges that turbulence RANS modelling for the blood flow in a stenotic carotid bifurcation is not an entirely settled topic. Although there seems to be consensus about the superiority of transitional RANS models, to the best of our knowledge no study is available in the literature to document and quantify the improvement of the results when moving from classical two-equations turbulence models to transitional models in a realistic, patient-specific geometry. To this purpose, a DNS carried out on the same anatomy is necessary to provide the reference solution upon which the critical evaluation of the turbulence models will be based.

It is the main goal of the present work to provide such quantification, by critically comparing a set of DNS results with those of various RANS models, all applied to the same realistic anatomy of a carotid artery bifurcation affected by a stenosis. The focus will be on the improvements made possible by a transitional model.

2 The geometrical model

With approval by the internal Technical Scientific Committee of the ICS Maugeri IRCCS Tradate, a standard computer tomography-angiography (CTA) of an adult male patient is used to build a 3-dimensional model of the carotid vessel. Figure 1 shows a sagittal section of the CTA: the presence of the contrast medium increases the radiodensity of blood and allows to easily distinguish the vessels from the surrounding tissues.

The segmentation process is carried out with the open-source software 3D Slicer [38]. The carotid artery is first separated from the rest of the CTA. Minor vessels (interested by a small fraction of the flow rate) are then removed, and the geometry is eventually exported in the STL format. The final result is shown on the right of Fig. 1, where the com-
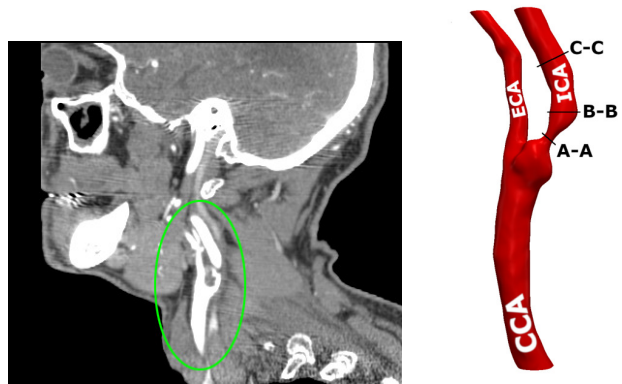

Fig. 1: Left: sagittal section of the CTA, with the carotid artery highlighted in white by the contrast medium. Right: the vessel geometry employed in the present work, showing the stenosed section A–A.
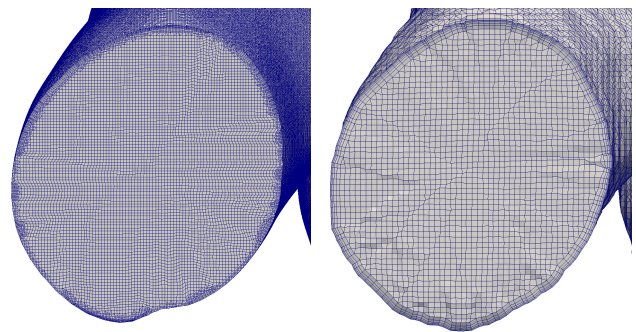

Fig. 2: Inlet section of the volume mesh at the CCA, for DNS (left) and RANS (right).

mon carotid artery (CCA) is visible in the lower part, the external carotid artery (ECA) on the upper left and the internal carotid artery (ICA) with an evident stenosis on the upper right. Although simplified to some extent, this patient-specific geometry is used in the rest of the work as a realistic testbed to assess the blood flow dynamics.

2.1 Mesh generation

Two different meshes are produced, one suitable for the DNS and one for the RANS simulations.

A uniform background mesh is created first by defining a parallelepiped containing the STL file, and then subdividing it into an appropriate number of cubic cells. Although very simple, the construction of the background mesh is important because it affects quality and quantity of the cells obtained at the end of the meshing procedure. The three-dimensional mesh that approximates, according to suitably specified parameters, the STL surface is then created by adding a number of layers near the solid boundaries, a step particularly important for the (coarser) RANS mesh, owing to the nature of the RANS models employed, which demand the first computational cell being well embedded within the viscous layer.

Figure 2 shows the inlet section of the CCA for both meshes, and vividly shows how the DNS mesh is much finer.

Table 1 summarizes some information about the quality of the two meshes obtained: the RANS mesh has approximately 1.35 million cells, whereas the DNS mesh has more than 30 million cells. Table 1 reports quantitative information about the two meshes, including the maximum values of parameters related to the quality of the mesh. The RANS mesh is designed to yield a problem of reasonable computational size, whereas the rationale behind the design of the DNS mesh is discussed below.

3 The numerical approach

In this work four numerical simulations are carried out on the same anatomy. The first one is a DNS, used for reference, while the remaining three are RANS simulations employing eddy-viscosity-type turbulence models to account for the effects of turbulence on the mean velocity and pressure fields. Two models are classic two-equations models, and the third is a transitional model, that is supposed to deal better with flows where turbulence is localized, either spatially or temporally. The rheological model of the fluid, the treatment of the wall and the boundary conditions are identical. All the simulations are performed with the open-source finite-volume solver OpenFOAM, version 2.3.0.

3.1 Numerical schemes

The mathematical modelling of the blood flow is based on the incompressible Navier–Stokes equations which, for a Newtonian fluid without body forces, read:

$$\nabla \cdot \mathbf{V} = 0 \tag{1a}$$

$$\frac{\partial \mathbf{V}}{\partial t} + (\mathbf{V} \cdot \nabla)\mathbf{V} + \frac{1}{\rho}\nabla p = \nu\nabla^2\mathbf{V} \tag{1b}$$

where $\mathbf{V}$ and p are velocity and pressure, $\nu = \mu/\rho$ is the kinematic viscosity (ratio of dynamic viscosity and density). A second-order linear scheme is employed for the discretization of the gradient operator and a Gauss linear corrected scheme for the Laplacian term in the momentum equation. The discretization of the non-linear terms of the momentum equation is carried out with a Gauss linear scheme for the DNS, while a Gauss upwind scheme is used for the RANS simulations to achieve convergence. All the simulations use a second-order backward difference formula for the temporal discretization.

3.2 Rheological model and treatment of the vessel walls

It is well known that blood in oscillatory flow may exhibit non-Newtonian characteristics, such as shear thinning, tixotropy and viscoelasticity [39–41]. However, the assumption of Newtonian fluid is generally accepted [42] when dealing with large arteries. This is corroborated also by [43], who evaluated the effects of different rheological models on the results of CFD simulations on a patient-specific (non stenotic) geometry, and concluded that the uncertainties related to the constitutive relation of the fluid are smaller than
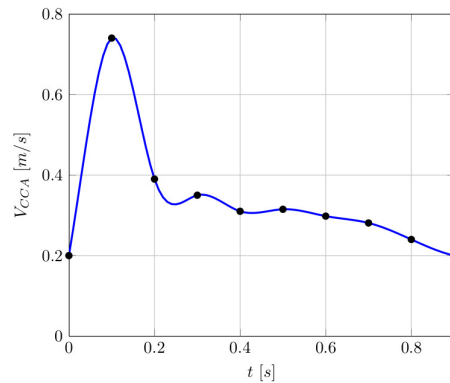

Fig. 3: Patient-specific temporal waveform of the blood flow velocity at the center of CCA, as obtained from *in-vivo* ultrasound measurements.

those deriving from the reconstruction of the geometry. The same conclusion was obtained in [17] with a laminar simulation. Hence, in our simulations blood is considered a Newtonian fluid with kinematic viscosity $\nu = 3.8 \cdot 10^{-6} m^2/s$.

In [42] as well as in [44], it is also mentioned that the compliance of the vessel walls only marginally affects the results, in comparison with the uncertainty on geometry. Furthermore, the presence of an atherosclerotic plaque causes a hardening of the vessel walls (the meaning of the term atherosclerosis is precisely "hardening" or "loss of elasticity"), such that in a stenosed vessel the assumption of rigid walls is even more reasonable. Hence, in our simulations the vessel walls are considered rigid.

3.3 Boundary conditions

Boundary conditions must be specified at four different portions of the computational domain: the inlet (CCA), the two outlets (ECA and ICA) and the vessel walls.

For the inlet section, *in vivo* velocity measurements at the CCA of the patient, acquired by means of ultrasound technique, are available during one cardiac cycle, lasting $T = 0.9s$, as shown in Fig. 3 where the systolic peak is at $t = 0.1s$, and the diastolic minimum at $t = 0s$ and $t = 0.9s$.

Although the inlet flow is laminar, assuming a parabolic shape for the inlet velocity profile, as taken from the Hagen-Poiseuille solution valid for an infinite cylindrical pipe, may be an oversimplification, owing to the flow unsteadiness. The relative importance of the unsteady forces with respect to the viscous forces in cylindrical pipe flow is expressed by the Womersley number α. When α is small, viscous forces dominate, the velocity profile is parabolic, and the centerline velocity oscillates in phase with the driving pressure gradient [45]. At the inlet section the Womersley number computed for a cylindrical pipe whose diameter D equates the hydraulic diameter of the CCA is:

$$\alpha = \frac{1}{2}D\sqrt{\frac{2\pi}{\nu T}} = 5.04. \tag{2}$$

Since $\alpha = 5.04$ is not necessarily small, the CCA inlet pro-

4   Copyright © by ASME

	Nodes	Faces	Cells	Max. Aspect Ratio	Max. non orthogonality	Average non orthogonality	Max. skewness
DNS	32 108 376	92 401 932	30 252 836	19.9	64.9	5.5	2.1
RANS	1 447 647	4 120 075	1 344 073	13.6	39.9	6.6	2.2

Table 1: Parameters of the finer mesh used for the DNS simulation, and the coarser one used for the RANS simulations.

	inlet	outlet	walls
Pressure	*zeroGrad*	zero	*zeroGrad*
Velocity	Womersley	*zeroGrad*	zero
k	$k = \frac{3}{2}(0.015 \cdot u)^2$	*zeroGrad*	zero
k_L	zero	*zeroGrad*	zero
ε	$\varepsilon = C_k^{3/2}/\ell_m$	*zeroGrad*	*zeroGrad*
ω	$\omega = C_k^{1/2}/\ell_m$	*zeroGrad*	*zeroGrad*

Table 2: Boundary conditions employed in the present work for pressure and velocity; turbulence variables are only used in the RANS calculations.

file is taken to be the Womersley profile, corresponding to the analytical solution of fully developed pulsatile laminar flow in a circular pipe [45]. Moreover, the profile is tilted to align with the local orientation of the CCA axis. The remaining boundary conditions are quite standard, and they are summarized in table 2. The near-wall region is resolved without resorting to wall functions, as the mesh is designed to have the first cell well within the buffer layer ($y^+ < 1$). A special remark is in order for the outlet condition. Although more detailed approaches are possible, we have decided to employ the simple outflow condition that is very popular in CFD applications. In fact, in several previous studies even simpler approaches were used, see for example the DNS study in Ref. [37], where a predetermined 59:41 partitioning of the flow rate between ECA and ICA is enforced. In our DNS and RANS simulations the flow rate partition is allowed to change during the beat, and indeed assumes slightly varying values of $58\% - 61\%$ in the ECA and $39\% - 42\%$ in the ICA.

3.4 Computational details

The simulations are carried out on the cluster GALILEO of the CINECA Italian Supercomputing Center. The unsteady PIMPLE solver is used to simulate 8 cardiac cycles. The 3 RANS cases are initialized with the result of a steady RANS simulation carried out with the SIMPLE solver. To remove any influence from the initial conditions, the first simulated cycle (either RANS and DNS) is discarded when evaluating statistics.

The RANS cases took $25h$ and $35h$ on 36 cores for the classic and transitional RANS respectively. Hence clas-

sic RANS models are computationally cheaper by approximately 30% for a given mesh size. The DNS required $250h$ on 144 cores to simulate one cardiac cycle. The number of simulated cycles in DNS is 8 (including the initial one), which is similar to [37], where 6 cardiac cycles were employed.

4 Turbulence models

The dynamics of an incompressible flow of a Newtonian fluid is fully described by the Navier–Stokes equations (1). The presence of turbulence in the blood flow is accounted for in the present work via two alternative approaches: either the whole range of dynamically relevant spatio-temporal scales of motion is solved with DNS, or the RANS equations in conjunction with turbulence modelling are solved at a reduced computational cost.

In the present study the DNS simulation is used as a reference to evaluate the modelling error introduced by the various turbulence models. The following sections briefly describe the main characteristics of the two approaches.

4.1 DNS

The DNS performed in this work may be defined as a quasi-DNS (q-DNS). The notion of q-DNS is intended as in [46], which assessed the capabilities of this approach for arbitrary polyhedral meshes. In a flow as complex as the present one, it is not trivial to rigorously establish the adequacy of a mesh to resolve all the spatial scales, short of carrying out costly mesh-refinement studies. Our approach is that of adopting a fine enough mesh to yield a DNS-like resolution, while at the same time employing (and bearing the cost of) a subgrid-scale LES turbulence model. The LES model is expected to affect the simulation only marginally, through very small values of the subgrid-scale turbulent viscosity, provided the mesh is sufficiently fine. The advantage of the present approach is two-fold: it provides a backup should the resolution become marginal in some regions of the computational domain and at some phases of the cycle, and it lends itself to a straightforward *a posteriori* verification of the adequacy of the spatial resolution.

The q-DNS mesh is designed on the basis of the following considerations. The most convenient Reynolds number to describe transition in pipe flow [47] is based on the bulk velocity, i.e. the mean volumetric flow rate divided by the cross-sectional of the vessel, and the hydraulic diameter. The

cycle maximum value of Re_b at the inlet is $Re_{b,in}^{\max} = 1040$ at $t = 0.1s$. The largest value of Re_b in the whole domain takes place at the section B–B of fig.1, where $D_h = 3.23mm$, and is $Re_{b,A-A}^{\max} = 1136$.

The q-DNS mesh used in this work consists of about 130 cells over the diameter at the section A−A. In order to get a qualitative feeling for the adequacy of the spatial resolution, we mention that the DNS of a turbulent flow in a cylindrical straight pipe at $Re_b = 4600$ requires 96 mesh points over the radius of the pipe section [48, 49] to properly resolve all the scales of motion. In other words, with a 4-times larger Re and a fully turbulent regime only 50% more points were used in the radial direction (which is the most demanding one in terms of spatial resolution), which suggests that the present mesh is sufficiently refined. It is worth mentioning again that the quantitative analysis of the subgrid-scale viscosity introduced by the LES model in the whole domain will make it possible to verify these estimates *a posteriori* (see fig.4 and related discussion below), thus confirming the adequacy of the present mesh.

Although the LES turbulence model employed in this simulation will be shown to have little to no effect on the results, its main characteristics are briefly reported below. The LES modeling starts from a decomposition between the resolved large scales and the modelled small (or sub-grid) scales:

$$\mathbf{u}(\mathbf{x},t) = \tilde{\mathbf{u}}(\mathbf{x},t) + \mathbf{u}'(\mathbf{x},t)$$

where the operator $\tilde{}$ is a low-pass filter.

In the filtered incompressible Navier–Stokes equations, the residual stress tensor τ_{ij}^r appears, which is expressed after the model introduced by Smagorinsky [50]:

$$\tau_{ij}^r = -2\nu_{sgs}(\mathbf{x},t)\tilde{S}_{ij}. \tag{3}$$

$\tilde{S}_{ij}$ is the filtered shear field, and the subgrid-scale viscosity $\nu_{sgs}(\mathbf{x},t)$ is defined as:

$$\nu_{sgs}(\mathbf{x},t) = (C_s\Delta)^2\sqrt{2\tilde{S}_{ij}\tilde{S}_{ij}} \tag{4}$$

where Δ is the mesh length scale, and $C_s = 0.17$ is a model constant.

The local and instantaneous value of the subgrid-scale viscosity $\nu_{sgs}(\mathbf{x},t)$, proportional to the square of the mesh length scale, determines the magnitude of the residual stresses, and provides a proxy to assessing how much the LES model affects the results. During the cardiac cycle, the maximum value of $\nu_{sgs}(\mathbf{x},t)$ is found to be $1.032 \cdot 10^{-6}m^2s^{-1}$, while an average over the cycle and the spatial domain gives $\nu_{sgs}(\mathbf{x},t) = 2.1 \cdot 10^{-8}m^2s^{-1}$. The mean maximum value over the whole cycle is $5.322 \cdot 10^{-7}m^2s^{-1}$. These values are respectively $27.2\%, 0.57\%$ and 14.03% of the blood molecular viscosity ν, confirming that the mesh is sufficiently refined, and that the present simulation can
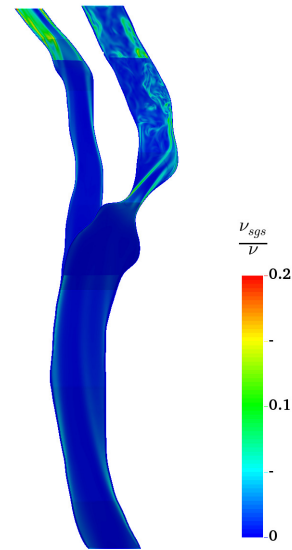

Fig. 4: Ratio $\nu_{sgs}(\mathbf{x},t)/\nu$ at $t = 0.1s$ of a generic cardiac cycle. Non-negligible values are visible only in the post-stenotic region and in the final part of the ECA, but these values are smaller than 1. The visible step changes (e.g. near the outlet sections) are due to mesh density changes.

be rightfully considered a q-DNS. Figure 4 shows the ratio $\nu_{sgs}(\mathbf{x},t)/\nu$ at $t = 0.1s$ of a generic cardiac cycle, i.e. at the most demanding phase, and confirms that even at this phase the value of the ratio is always significantly smaller than 1.

4.2 RANS models

The RANS approach avoids the solution of the time-dependent Navier–Stokes equations, and resorts to the so-called Reynolds' decomposition of the velocity (and pressure) field:

$$\mathbf{u}(\mathbf{x},t) = \overline{\mathbf{u}}(\mathbf{x}) + \mathbf{u}'(\mathbf{x},t)$$

where $\overline{\mathbf{u}}(\mathbf{x})$ is the mean velocity field obtained by applying the time averaging operator to $\mathbf{u}(\mathbf{x},t)$:

$$\overline{\mathbf{u}}(\mathbf{x}) = \lim_{T\to+\infty}\frac{1}{T}\int_0^T \mathbf{u}(\mathbf{x},t)\,dt.$$

The flow of interest (the cardiac cycle) is clearly time-dependent; as such, it requires the solution of the unsteady Reynolds-averaged Navier–Stokes equations (URANS), where the mean velocity field retains a residual dependence upon time. In this case, one assumes that two well separated time scales T_1 and $T_2 \gg T_1$ exist in the flow. The Reynolds' averaging operator can be thus redefined as:

$$\overline{\mathbf{u}}(\mathbf{x},t) = \frac{1}{T}\int_{-T/2}^{T/2} \mathbf{u}(\mathbf{x},t+t')\,dt' \quad T_1 \ll T \ll T_2$$

The URANS equations are obtained by using this averaging operator:

$$\nabla \cdot \overline{\mathbf{u}} = 0 \tag{5a}$$

$$\rho \frac{\partial \overline{\mathbf{u}}}{\partial t} + \rho \nabla \cdot (\overline{\mathbf{u}\mathbf{u}}) + \nabla \overline{p} + \nabla \cdot \overline{\mathbf{J}_{\mathbf{Q}}^d} = 0 \tag{5b}$$

where $\overline{\mathbf{J}_{\mathbf{Q}}^d}$ is the dissipative part of the stress tensor which for Newtonian fluids can be written as:

$$\overline{J_{\mathbf{Q},ij}^d} = -\mu \left(\frac{\partial \overline{u}_i}{\partial x_j} + \frac{\partial \overline{u}_j}{\partial x_i} \right).$$

The non-linear term $\overline{\mathbf{u}\mathbf{u}}$ in eq. (5b) can be rewritten as:

$$\overline{\mathbf{u}\mathbf{u}} = \overline{\mathbf{u}}\,\overline{\mathbf{u}} + \overline{\mathbf{u}'\mathbf{u}'}.$$

The quantity $\mathbf{R} = \rho \overline{\mathbf{u}'\mathbf{u}'}$ is called Reynolds stress tensor, and a total stress tensor $\mathbf{T}$ is introduced as:

$$\mathbf{T} = \overline{\mathbf{J}_{\mathbf{Q}}^d} + \mathbf{R}$$

Therefore eq. (5b) becomes:

$$\rho \frac{\partial \overline{\mathbf{u}}}{\partial t} + \rho \nabla \cdot (\overline{\mathbf{u}}\,\overline{\mathbf{u}}) + \nabla \overline{p} + \nabla \cdot \mathbf{T} = 0 \tag{6}$$

The equations just obtained cannot determine the mean velocity field $\overline{\mathbf{u}}$ as the link between $\overline{\mathbf{u}}$ and $\mathbf{R}$ does not exist. Closure of the problem can be achieved with the Bousinnesq assumption:

$$R_{ij} = -2\nu_t \overline{S}_{ij}$$

which states that every component R_{ij} of the Reynolds stress tensor is proportional to the tensor $\overline{\mathbf{S}}$ of components:

$$\overline{S}_{ij} = \frac{1}{2} \left(\frac{\partial \overline{u}_i}{\partial x_j} + \frac{\partial \overline{u}_j}{\partial x_i} \right)$$

The proportionality factor ν_t, function of the position $\mathbf{x}$, is the eddy viscosity, and the various models differ in the way ν_t is calculated.

The main features of the two well-known and commonly used two-equations models employed in the present work are described below, followed by the transitional $k_T - k_L - \omega$ model.

4.2.1 The $k - \varepsilon$ model

The $k - \varepsilon$ model uses one differential transport equation for the turbulent kinetic energy k, and another for its dissipation rate ε, complemented by an algebraic constitutive relation linking ν_t to k and ε. The variant employed here is that described in [51], where the selection of the numerical values of the various model constants is improved compared to the original version [52].

The model equation for k is:

$$\frac{Dk}{Dt} = \mathscr{P}_k - \varepsilon + \frac{\partial}{\partial x_j} \left[\left(\nu + \frac{\nu_t}{\sigma_k} \right) \frac{\partial k}{\partial x_j} \right] \tag{7}$$

where $D/Dt(\cdot) \equiv \partial/\partial t(\cdot) + \overline{u}_i \partial/\partial x_i(\cdot)$ is similar to a material derivative, σ_k is a model constant, and $\mathscr{P}_k$ is the production rate of k, given by:

$$\mathscr{P}_k = 2\nu_t \overline{S}_{ij} \overline{S}_{ij}$$

The model equation for ε descends from the previous Eq.(7) multiplied by ε/k, and is:

$$\frac{D\varepsilon}{Dt} = C_{1\varepsilon} \frac{\varepsilon}{k} \mathscr{P}_k - C_{2\varepsilon} \frac{\varepsilon^2}{k} + \frac{\partial}{\partial x_j} \left[\left(\nu + \frac{\nu_t}{\sigma_\varepsilon} \right) \frac{\partial \varepsilon}{\partial x_j} \right] \tag{8}$$

where $C_{1\varepsilon}$, $C_{2\varepsilon}$ and σ_ε are model constants. Once equations (7) and (8) are solved, the eddy viscosity is obtained via the constitutive equation:

$$\nu_t = C_\mu \frac{k^2}{\varepsilon}. \tag{9}$$

4.2.2 The $k - \omega$ model

The $k - \omega$ model developed by Wilcox in [53] utilizes an equation for ω (interpreted as the turbulence frequency, and linked to the other turbulence variables by the relation $\omega = \varepsilon/k$) instead of the equation for ε. The equation for k has the same structure of equation (7) and is written as:

$$\frac{Dk}{Dt} = \mathscr{P}_k - \beta^* \omega k + \frac{\partial}{\partial x_j} \left[(\nu + \alpha_k \nu_t) \frac{\partial k}{\partial x_j} \right]. \tag{10}$$

The model equation for ω is:

$$\frac{D\omega}{Dt} = \alpha \frac{\omega}{k} \mathscr{P}_k - \beta \omega^2 + \frac{\partial}{\partial x_j} \left[(\nu + \alpha_\omega \nu_t) \frac{\partial \omega}{\partial x_j} \right] \tag{11}$$

Once equations (10) and (11) are solved, the eddy viscosity is calculated as:

$$\nu_t = \frac{k}{\omega}$$

Tables 3 and 4 show the employed values of the model constants for $k - \varepsilon$ and $k - \omega$ respectively.

$C_{1\varepsilon}$	$C_{2\varepsilon}$	C_μ	σ_k	σ_ε
1.44	1.92	0.09	1.0	1.3

Table 3: Values of the constant in the $k - \varepsilon$ model, after [51]

β^*	β	α	α_k	α_ω
0.09	0.072	0.52	0.50	0.50

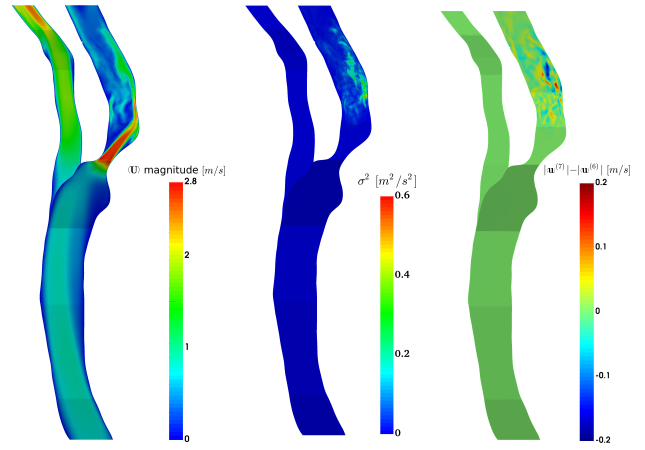Table 4: Values of the constants in the $k - \omega$ model, after [53]

Fig. 5: Phase-averaged magnitude of the velocity vector (left) and its temporal variance (center) at $\tau = 0.1s$. The ensemble average is performed over 7 cycles, and the temporal variance gives an hint of the statistical error associated to the estimate of the expected value of the mean. On the right, difference between the mean velocity field $|\langle \mathbf{u} \rangle^{(7)}|$ obtained averaging over 7 cycles, and the same quantity obtained over 6 cycles.

4.3 The transitional $k_T - k_L - \omega$ model

The transitional RANS model considered in this work is the $k_T - k_L - \omega$ model developed in [54], as a followup of [55]. It is based on the idea of bypass transition, according to which transition to turbulence is related to the amplification of streamwise fluctuations generated in the pre-transitional region of a boundary layer [56]. These fluctuations are not strictly turbulent, and the concept of laminar kinetic energy k_L is useful to describe their development till transition. For this reason, a third model equation for k_L is adopted in addition to the equations for ω and the turbulent kinetic energy k_T. The fluctuations in the pre-transitional region are subject to amplification when the dynamics of turbulence production is sufficiently fast in comparison to that of molecular diffusion. Therefore, the transition process is started when the ratio between the temporal scales of turbulence production and molecular diffusion reaches a critical value. The 3 model equations are reported below:

$$\frac{Dk_T}{Dt} = \mathscr{P}_{k_T} + \mathscr{R}_B + \mathscr{R}_N - \omega k_T - \mathscr{D}_T +$$
$$+ \frac{\partial}{\partial x_j}\left[\left(\nu + \frac{\alpha_T}{\alpha_k}\right)\frac{\partial k_T}{\partial x_j}\right] \quad (12a)$$

$$\frac{Dk_L}{Dt} = \mathscr{P}_{k_L} - \mathscr{R}_B - \mathscr{R}_N - \mathscr{D}_L +$$
$$+ \frac{\partial}{\partial x_j}\left[\nu \frac{\partial k_L}{\partial x_j}\right] \quad (12b)$$

$$\frac{D\omega}{Dt} = C_{\omega 1}\frac{\omega}{k_T}\mathscr{P}_{k_T} + \left(\frac{C_{\omega R}}{f_W} - 1\right)\frac{\omega}{k_T}\left(\mathscr{R}_B + \mathscr{R}_N\right) -$$
$$- C_{\omega 2}\omega^2 + C_{\omega 3}f_\omega \alpha_T f_W^2 \frac{\sqrt{k_T}}{d^3} +$$
$$+ \frac{\partial}{\partial x_j}\left[\left(\nu + \frac{\alpha_T}{\alpha_\omega}\right)\frac{\partial \omega}{\partial x_j}\right]. \quad (12c)$$

In the equation for ω the production, dissipation and diffusion terms (respectively the first, third and fifth term on the right side of eq. (12c)) are in parallel with the analogous terms of the equation for k_T and k_L. The turbulent kinetic energy is now:

$$k = k_T + k_L \quad (13)$$

The transition process is modeled through a transfer of energy from k_L to k_T. The terms $\mathscr{R}_B$ and $\mathscr{R}_N$ have opposite sign in the equations (12a) and (12b) and represent the bypass transition and natural transition phenomena respectively. Further information about the terms in equations (12) and values of the constants can be found in the above mentioned paper [54].

5 DNS results

The results of the q-DNS need to be interpreted in a statistical sense if a comparison with time-averaged RANS results has to be made. Hence, the phase-averaging operator is introduced to carry out an ensemble average over the available cardiac cycles; it is defined for the generic quantity ϕ at a point $\mathbf{x}$ in the computational domain as follows:

$$\langle \phi \rangle(\mathbf{x}, \tau) = \frac{1}{N}\sum_{n=0}^{N-1} \phi(\mathbf{x}, \tau + nT)$$

where $N = 7$ is the number of cycles used for estimating the mean, $T = 0.9s$ is the period of the cycle, and $0 \le \tau \le 0.9s$.

The standard deviation of ϕ at each point in space $\mathbf{x}$ is

8

defined as:

$$\sigma(\mathbf{x}, \tau) = \sqrt{\frac{1}{N} \sum_{n=0}^{N-1} [\phi(\mathbf{x}, \tau + nT) - \langle\phi\rangle(\mathbf{x}, \tau)]^2}$$

Fig. 5 plots the fields of the phase-averaged velocity magnitude at $\tau = 0.1s$ (corresponding to the systolic peak, see Fig. 3) and its variance σ^2, on the mid-plane of the carotid bifurcation. On the right panel, the difference in the phase-averaged mean field is plotted when computed with $N = 7$ cycles and with $N = 6$; this difference is instrumental to appreciating the level of convergence of the estimate of the mean, when only 7 samples are available.

The mean field (Fig. 5 left) emphasizes the strong jet exiting the stenotic section, with a magnitude of the local velocity up to 2.8 m/s. The jet impacts the vessel wall shortly downstream of the stenosis, where a vast low-momentum region can be appreciated. The region where the mean velocity shows irregular features is limited to the portion of the ICA downstream of the stenosis, pointing at the presence of a turbulent and highly fluctuating flow, together with a possible residual statistical error in the estimate of the mean due to the small number of samples.

The statistical error associated with the averaging procedure is hinted at by the examination of the variance field, which will be used later on to assess the validity of the comparison between the DNS and the RANS simulations discussed in the next section. The variance of the magnitude of the mean velocity vector is shown in Fig. 5 (center), and allows us to compute the standard error (SE) of our estimate of the mean value. The SE of the mean is the standard deviation of the sample mean, which is an estimate of the population mean. The standard error is usually estimated by the sample estimate of the population standard deviation (sample standard deviation) divided by the square root of the sample size (for further information see [57]). At $\tau = 0.1s$ the largest variance is $\sigma^2_{max} = 0.5746 \ m^2/s^2$, and the largest SE associated to the mean velocity can be estimated as

$$SE = \frac{\sigma_{max}}{\sqrt{N}} = 0.286 \ \frac{m}{s}, \tag{14}$$

where $N = 7$ is the number of samples.

It is interesting to observe that this numerical value is quite close to the value of the largest difference in the mean velocity field that is obtained by removing the last sample. In fact, fig. 5 (right) plots the spatial distribution of the difference between the magnitude of the phase-averaged velocity field at $\tau = 0.1s$ obtained averaging over seven cardiac cycles, i.e. $|\langle\mathbf{u}\rangle^{(7)}|$ and the same quantity obtained with six cycles, i.e. $|\langle\mathbf{u}\rangle^{(6)}|$. Differences can be appreciated only in the post-stenotic region, with a maximum value of 0.203 m/s. This is a relatively small value, considering that at this phase of the cycle the mean velocity magnitude can be larger than 2.8 m/s. Moreover, the pre-stenotic region and the flow in the ECA are almost unaffected by the limited sample size.
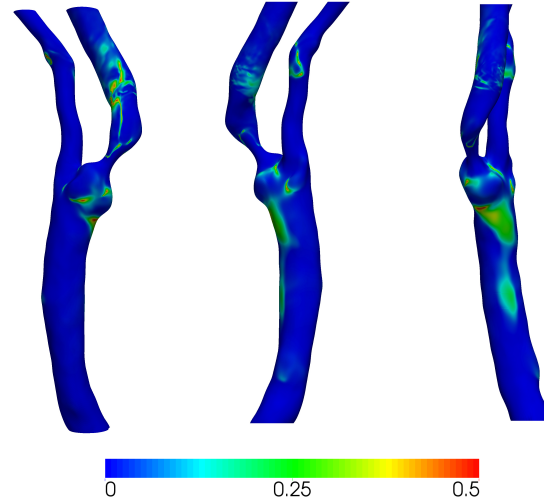

Fig. 6: Spatial distribution of the OSI index, as computed from DNS, viewed from three different angles. Significant oscillations of the WSS vector are observed in localized portions of the post-stenotic region, in areas just upstream of the carotid bifurcation, and in a small area in the final part of the ECA.

Hence, in line with [37], the use of 7 actual cycles is considered a good compromise between the need for an accurate statistical description of the flow and the requirement of an affordable computational cost.

We further present in fig. 6 the behavior of the Oscillatory Shear Index (OSI), a quantity often used in the literature to quantify the importance of the unsteady wall-shear stresses (WSS). The OSI describes the cyclic departure of the WSS vector from its predominant axial alignment [58, 59]. The OSI is a wall-based and time-independent scalar quantity defined as follows (using phase-averaged values in the case of DNS):

$$OSI = \frac{1}{2}\left(1 - \frac{|\int_0^T \langle WSS\rangle \, dt|}{\int_0^T |\langle WSS\rangle| \, dt}\right).$$

The WSS vector is calculated as:

$$WSS = \nu\nabla\mathbf{u}\cdot\mathbf{n}$$

where $\mathbf{n}$ is the direction perpendicular to the vessel surface. By its definition, the OSI ranges from 0 to 0.5, where a value of 0 means that the instantaneous WSS vector is always aligned with the time-averaged vector throughout the entire pulse and, thus, does not oscillate at all. On the other hand, 0.5 means that the instantaneous vector is never aligned with the time-averaged vector, thus indicating an extremely oscillating behavior. The importance of the OSI and the ability of its correct prediction via numerical simulations resides in the direct link between OSI and the process of rupture of the atherosclerotic plaque [60].
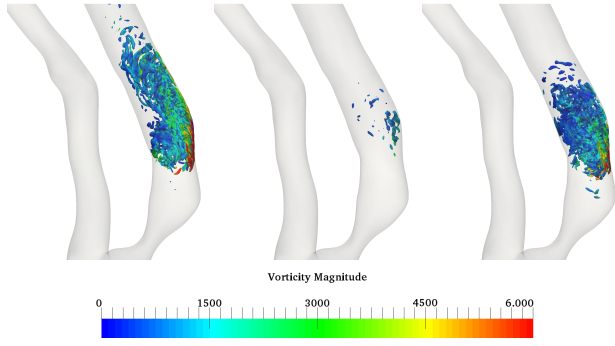
9

Fig. 7: Isosurfaces for $\lambda_2 = -250000\ s^{-1}$, colored by the vorticity magnitude, in an instantaneous flow field at different phases of the cycle: $\tau = 0.1$, left; $\tau = 0.2$, center; $\tau = 0.3$, right. The color scale is expressed in $1/s$. Turbulent structures are present downstream of the stenosis mainly between $t = 0.1s$ and $t = 0.2s$.

The OSI can be easily calculated as a post-processing of DNS results, and it is shown in fig. 6. The DNS results produce large values of the OSI in a few patches of the post-stenotic region, as well as in a few areas just upstream of the carotid bifurcation. Oscillations of the WSS vector are also present in a small area located in the final part of the ECA.

Finally, we use the fluctuating velocity field $\mathbf{u}'$ to compute the quantity λ_2, which is often employed [61] to visualize vortical regions in the flow, identified by regions where λ_2 is negative. We seek further evidence to the fact that the flow is not turbulent everywhere and at every time, something that has profound implications on turbulence modeling.

The scalar quantity λ_2 is defined as the second eigenvalue of the symmetric tensor $\mathbf{S}^2 + \mathbf{A}^2$ where:

$$\mathbf{S} = \frac{1}{2}\left(\nabla\mathbf{u}' + (\nabla\mathbf{u}')^T\right)$$

and

$$\mathbf{A} = \frac{1}{2}\left(\nabla\mathbf{u}' - (\nabla\mathbf{u}')^T\right)$$

are the symmetric and anti-symmetric part of the tensor $\nabla\mathbf{u}'$ [62]. Figure 7 shows isosufaces of λ_2 at three different phases of a cycle, i.e. $\tau = 0.1\ s$, $\tau = 0.2\ s$ and $\tau = 0.3\ s$. It is evident that turbulent structures appear quite downstream of the stenosis, especially in the time interval between the systolic peak (fig. 7 left) and the end of the deceleration phase (fig. 7 center), while in the remaining parts of the domain no structures can be seen. At $\tau = 0.3\ s$ (fig. 7 right) the vortical structures begin to disappear and after that time the flow appears to be nearly laminar even in the ICA. This confirms that, in a real carotid artery affected by stenosis, turbulence is present only at certain phases of the cardiac cycle, and only in the post-stenotic region. For this reason, a turbulence model capable to describe the transition (both in space and time) from the laminar to the turbulent regime is expected
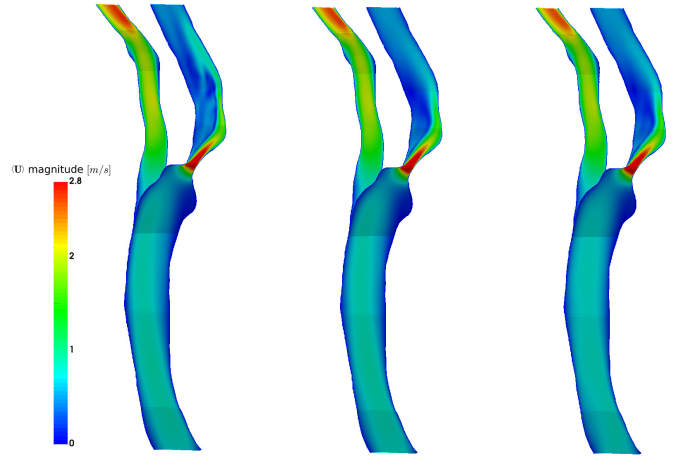

Fig. 8: Magnitude of the mean velocity vector as computed by the RANS models at $\tau = 0.1s$: $k - k_L - \omega$ model (left), $k - \varepsilon$ model (center), $k - \omega$ model (right). Quantities are plotted in the mid-plane of the carotid bifurcation. By comparison with fig. 5 (left), the transitional model is seen to be much better at reproducing the complex flow pattern in the post-stenotic region after the jet impacts the vessel wall.

to possess particularly good predictive characteristics for the flow under consideration.

6 Comparison between DNS and RANS

Once the DNS database is available, the phase averaging procedure allows isolating the background turbulent velocity fluctuations from the mean velocity field. The latter is used to carry out a first comparison between RANS and DNS calculations. Figure 8 shows the magnitude of the mean velocity field, plotted in the mid-plane of the carotid bifurcation, predicted by the RANS models at $\tau = 0.1s$. Although at first glance the 3 plots may seem qualitatively similar, a comparison with figure 5 (left) reveals that the transitional model better predicts the complex flow pattern present in the post-stenotic region after the strong jet exits the restriction and impacts the vessel walls. The two classic RANS models are unable to correctly reproduce the region with relatively large velocity close to the wall on the right, clearly underestimating the value of the mean velocity.

The phase averaging procedure of the DNS results also allows to compute the turbulent kinetic energy:

$$k = \frac{1}{2}\left[\left\langle u'^2 \right\rangle + \left\langle v'^2 \right\rangle + \left\langle w'^2 \right\rangle\right], \qquad (15)$$

for which every considered RANS model provides an explicit prediction. A simple comparison then brings to light the error incurred by the models. Fig. 9 plots, for every turbulence model, the difference between the RANS-predicted k and the DNS-computed k. The comparison is carried out in the mid plane of the artery bifurcation for two different phases of the cardiac cycle. It emerges that, at both the considered phases, the transitional turbulence model provides
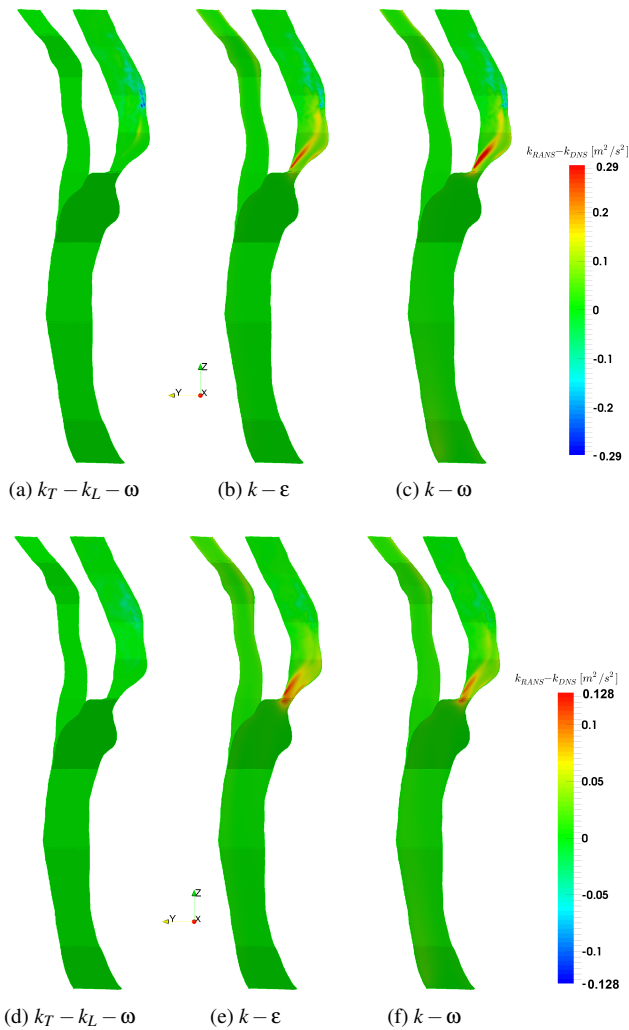
(a) $k_T - k_L - \omega$ (b) $k - \varepsilon$ (c) $k - \omega$

(d) $k_T - k_L - \omega$ (e) $k - \varepsilon$ (f) $k - \omega$

Fig. 9: Difference $k_{RANS} - k_{DNS}$ between the turbulent kinetic energy k_{RANS} predicted by the RANS models and the same quantity k_{DNS} computed by the DNS, shown at the mid plane of the artery bifurcation. Top: $\tau = 0.1s$; bottom: $\tau = 0.2s$. The transitional model (left) provides significantly better results overall, especially in the important region immediately downstream of the stenosis, where the two-equation models significantly overestimate the level of turbulent fluctuations.

significantly better results, with the whole field of k predicted with small error or no error at all, if exception is made for a few small spots at $\tau = 0.1\ s$ in the post-stenotic impingement region. On the other hand, the classic RANS models lead both to an incorrect prediction of k right at the stenosis and downstream, significantly overestimating the level of turbulent fluctuations.

At $\tau = 0.1\ s$ the region of the ICA downstream of the stenosis, and in particular the impingement region, appears to be difficult to deal with for both classic and transitional models. In fact, in this area the value of k is underestimated in small spots near the right wall. The value of the standard error at $\tau = 0.1\ s$ as calculated in eq. (14) is important in interpreting this aspect. In fact, the square of the SE associ-
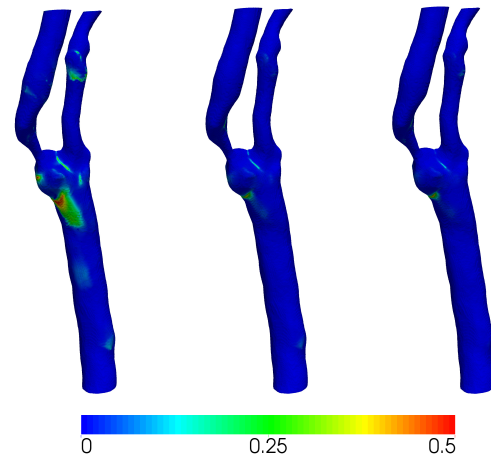

Fig. 10: OSI as computed from transitional (left), $k - \varepsilon$ (center) and $k - \omega$ (right) RANS models. If compared with fig. 6 (right), the transitional model is seen to much better reproduce the DNS results. Two-equations RANS model predict nearly zero OSI (non-oscillatory WSS) except for small regions upstream the carotid bifurcation.

ated with k can be quantified as $SE^2 = 0.082\ m^2/s^2$, a small value in comparison with the typical differences observed in figs. 9b, 9c and 9a. This observation is essential to confirm that the differences visible in figure 9 are related to actual differences in the k fields, and not just to the statistical error associated with finite-time averaging.

A further comparison based on the OSI is shown in Figs. 10 and 11. The first provides an overall view of the OSI surface field, and conveys the idea that the transitional model is vastly superior to the classic RANS models in predicting a spatial distribution of OSI that closely resembles the DNS one, both in terms of absolute values and location of the regions where the flow deviates from a non-oscillatory behavior. The distribution in the area just upstream the stenosis is well approximated by the transitional model, while the classic RANS models clearly underestimate the oscillations of the WSS vector. The same happens in the post-stenotic region, where the transitional model performs better than the classic RANS, although it does not fully succeed in accurately describing the complex pattern predicted by the DNS.

Figure 11 provides a detailed, zoomed view of the stenotic region, and confirms that the distribution in the ICA is well approximated only by the transitional model, that is able to capture the localized ridged peak of the OSI along the ascending branch.

As a final comparison, we examine the temporal behavior of pressure, spatially averaged over the sections B–B and C–C introduced in fig.1. Plotted in the graphs is the difference between the section-averaged pressure p_{av} and the external reference pressure p_{ext} outside the vessel walls. Obviously, in the DNS case pressure is also phase-averaged over the available cardiac cycles. The evolution over time, and in particular its minimum values, are important because, as recalled in the Introduction, negative pressure could lead to a
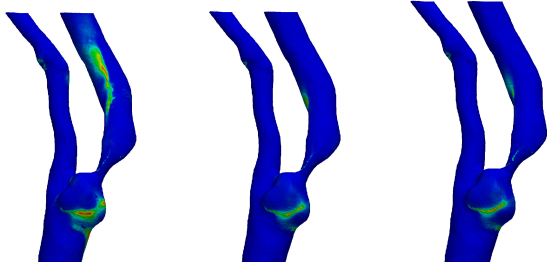
11

Fig. 11: OSI as computed from transitional (left), $k - \varepsilon$ (center) and $k - \omega$ (right) RANS models: zoom on the post-stenotic region. If compared with fig. 6 (left), the transitional model predicts oscillations in the post-stenotic region in accordance with the DNS result, but the complex pattern is not correctly reproduced. Two-equations RANS models significantly underestimate the extent of WSS vector oscillation in the post-stenotic region.
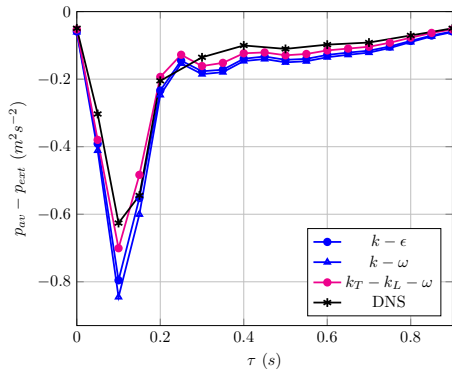

Fig. 12: Temporal evolution of the difference $p_{av} - p_{ext}$ between the section-averaged pressure p_{av} over the section B–B, as identified in fig. 1, and the external pressure p_{ext}. The negative pressure peak at $\tau = 0.1\ s$ is overestimated by all models, but the transitional model is significantly more accurate.
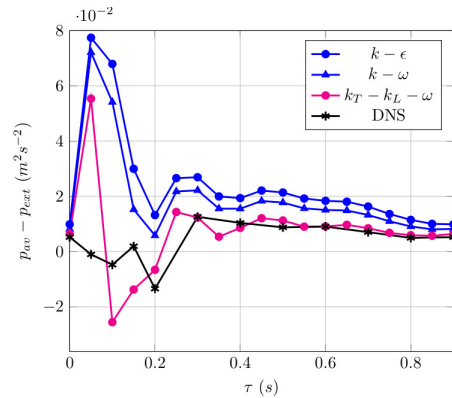

Fig. 13: Temporal evolution of the difference $p_{av} - p_{ext}$ between the section-averaged pressure p_{av} over the section C–C, as identified in fig. 1, and the external pressure p_{ext}. The $k_T - k_L - \omega$ points lie on the DNS curve after the systolic peak. Near the systolic peak at $\tau = 0.1\ s$ the transitional model is the only one to be not too far off the DNS values.

collapse of the vessel in correspondence of the stenosis.

None of the turbulence model provides entirely satisfactory predictions. The transitional model, however, consistently shows improved predictions compared to the standard two-equations models. In section B–B (fig. 12), slightly downstream of the stenosis, all the turbulence models underestimate the minimum value of pressure during the systolic phase ($\tau = 0.1\ s$), although the classic non-transitional models are off by more than twice the error observed for the transitional model. The difference between the DNS value and the RANS-computed values remains visible at later stages of the cycle, where pressure remains negative but decreases towards zero: RANS values are consistently lower than the DNS one, and the transitional model is the nearest to DNS.

In section C–C (fig. 13), located after the stenosis but also after the impingement region, the absolute values of pressure are lower, but the improvement brought about by the use of the transitional model is more evident. In fact, after $\tau = 0.2\ s$ the $k_T - k_L - \omega$ points practically lie on the DNS curve. Substantial differences are visible only at the systolic phase and immediately thereafter ($\tau = 0.1\ s$ and $\tau = 0.15\ s$), but also at these phases the transitional model better approximates the results of the DNS.

7 Conclusions

The blood flow in a stenosed, patient-specific, carotid bifurcation has been numerically simulated by solving the unsteady RANS equations. The aim of the study is to ascertain whether transitional RANS models, that consider the transition process from the laminar to the turbulent regime, are well suited in such an application, by providing significant improvements in solution accuracy at negligible additional computing cost. To quantify the improvements objectively, a companion DNS has been carried out on the same anatomy, thus providing for the first time a direct comparison of the outcome of standard and transitional RANS model in a patient-specific setting.

The DNS has been effective at describing the complexity of the flow, indicating that turbulent motions only exist at the beginning of the cardiac cycle near the systolic peak, and only downstream of the stenosed section. Hence turbulence is confirmed, in this specific flow, to be a localized phenomenon, both in space and time.

A comparison between DNS and RANS with different models has proved that the three-equation transitional model is definitely more accurate in describing the solution in terms of turbulence kinetic energy (which is severely overestimated by classic models, especially when and where the flow is nearly laminar), OSI and temporal evolution of the pressure. It is noteworthy that the classic models provide results which are in very good mutual agreement, while differing from those of the transitional model significantly. Hence the role of the accompanying DNS study on the same patient-specific anatomy is essential to identify and interpret such differences.

It should be remembered that transitional models bring along a (limited) computational overhead when compared to

12   Copyright © by ASME

the classic models. Although a comparison at the same computational cost has not been carried out, the present mesh is such that all models provide essentially mesh-independent results. Hence, the superiority of the transitional model is assessed, at least when reasonable mesh sizes are employed.

Even if the $k_T - k_L - \omega$ model used in this work is still not accurate enough to achieve a perfect description of the flow statistics as observed by the DNS, the class of transitional RANS models appears to be the correct choice for the type of simulations considered in the present work, where the flow is not fully turbulent. In order to improve the description of the flow in such simulations, more recent transitional models could be used. For example, the new $k - \omega - v2$ model recently developed [63] proposes an alternative to the laminar kinetic energy approach involved in the present work, and was proved to have more capabilities, especially for free shear flows.

The boost in solution accuracy envisaged by the use of transitional model, together with additional developments that have not been employed in the present work but are already or are becoming available (more accurate reconstruction of geometry, non-Newtonian rheological models, deformable walls, more physically consistent outlet boundary conditions) will pave the way for the use of patient-specific RANS simulations as a valuable tool in the clinical practice.

A certain amount of idealization clearly exists in the present study, as in the simplified anatomy, the assumption of rigid walls, some of the boundary conditions, and the rheological model. However, its focus is on the potential advantages of transitional RANS models versus the classic ones, which are often used in literature but cannot capture the transitional nature of the flow. Our work demonstrates that classic RANS models may provide incorrect estimates of important fluid dynamics quantities, whereas transitional models possess much better predictive capabilities at a comparable computational cost.

Conflict of interest statement

Acknowledgments

References

[1] Ross, R., 1993. "The pathogenesis of atherosclerosis: a perspective for the 1990s". *Nature,* **362**(6423), pp. 801–809.

[2] GBD 2013 Mortality and Causes of Death Collaborators, 2014. "Global, regional, and national age-sex specific all-cause and cause-specific mortality for 240 causes of death, 1990-2013: a systematic analysis for the Global Burden of Disease study 2013". *Lancet,* **385**(9963), 12/18, pp. 117–171.

[3] Towfighi, A., and Saver, J. L., 2011. "Stroke declines from third to fourth leading cause of death in the United States: historical perspective and challenges ahead". *Stroke,* **42**(8), pp. 2351–2355.

[4] Go, A. S. *et al*, 2013. "Heart disease and stroke statistics–2013 update". *Circulation,* **127**(1).

[5] Shaaban, A. M., and Duerinckx, A. J., 2000. "Wall shear stress and early atherosclerosis". *Am. J. Roentgenol.,* **174**(6), pp. 1657–1665.

[6] Gimbrone, M. J., Resnick, N., Nagel, T., Khachigian, L. M., Collins, T., and Topper, J. N., 1997. "Hemodynamics, endothelial gene expression, and atherogenesis". *Ann. New York Acad. Sci.,* **811**, pp. 1–10.

[7] Malek, A. M., Alper, S. L., and Izumo, S., 1999. "Hemodynamic shear stress and its role in atherosclerosis". *J. Am. Med. Assoc.,* **282**(21), pp. 2035–2042.

[8] Birchall, D., Zaman, A., Hacker, J., Davies, G., and Mendelow, D., 2006. "Analysis of haemodynamic disturbance in the atherosclerotic carotid artery using computational fluid dynamics". *Eur. Radiol.,* **16**(5), pp. 1074–1083.

[9] Cibis, M., Potters, W. V., Selwaness, M., Gijsen, F. J., Franco, O. H., Lorza, A. M. A., de Bruijne, M., Hofman, A., der Lugt van, Nederveen, A. J., and Wentzel, J. J., 2016. "Relation between wall shear stress and carotid artery wall thickening MRI versus CFD". *J. Biomech.,* **49**(5), pp. 735–741.

[10] Groen, H. C., Gijsen, F. J. H., der Lugt van, Ferguson, M. S., Hatsukami, T. S., der Steen van, Yuan, C., and Wentzel, J. J., 2007. "Plaque rupture in the carotid artery is localized at the high shear stress region". *Stroke,* **38**(8), p. 2379.

[11] Executive Committee for the Asymptomatic Carotid Atherosclerosis Study, 1995. "Endarterectomy for asymptomatic carotid artery stenosis". *J. Am. Med. Assoc.,* **273**(18), pp. 1421–1428.

[12] Tuenter, A., Selwaness, M., Lorza, A. A., Schuurbiers, J. C. H., Speelman, L., Cibis, M., der Lugt van, de Bruijne, M., der Steen van, Franco, O. H., Vernooij, M. W., and Wentzel, J. J., 2016. "High shear stress relates to intraplaque haemorrhage in asymptomatic carotid plaques". *Atherosclerosis,* **251**, pp. 348–354.

[13] Slack, S. M., Cui, Y., and Turitto, V. T., 1993. "The effects of flow on blood coagulation and thrombosis". *Thromb. Haemostasis,* **70**(1), pp. 129–134.

[14] Affeld, K., Reininger, A. J., Gadischke, J., Grunert, K., Schmidt, S., and Thiele, F., 1995. "Fluid mechanics of the stagnation point flow chamber and its platelet deposition". *Artificial Organs,* **19**(7), pp. 597–602.

[15] Paul, M. C., Molla, M. M., and Roditi, G., 2009. "LargeEddy simulation of pulsatile blood flow". *Med. Eng. Phys.,* **31**(1), pp. 153–159.

[16] Varghese, S. S., and Frankel, S. H., 2003. "Numerical modeling of pulsatile turbulent flow in stenotic vessels". *J. Biomech. Eng.,* **125**(4), pp. 445–460.

[17] Gharahi, H., Zambrano, B. A., Zhu, D. C., DeMarco, J. K., and Baek, S., 2016. "Computational fluid dynamic simulation of human carotid artery bifurcation

based on anatomy and volumetric blood flow rate measured with magnetic resonance imaging". *Int. J. Adv. Eng. Sci. Appl. Math.,* **8**(1), pp. 46–60.

[18] Khodarahmi, I., 2015. "Comparing velocity and fluid shear stress in a stenotic phantom with steady flow: phase-contrast MRI, particle image velocimetry and computational fluid dynamics". *Magma Magn. Reson. Mater. Phys. Biol. Med.,* **28**(4), pp. 385–393.

[19] Suri, J. S., Pattichis, C. S., Li, C., Macione, J., Yang, Z., Fox, M. D., Wu, D., and Laxminarayan, S., 2005. "Plaque imaging using ultrasound, magnetic resonance and computer tomography: a review". *Stud. Health Technol. Inform.,* **113**, pp. 1–25.

[20] Mittal, R., Simmons, S. P., and Udaykumar, H. S., 2001. "Application of large-eddy simulation to the study of pulsatile flow in a modeled arterial stenosis". *J. Biomech. Eng.,* **123**(4), pp. 325–332.

[21] Molla, M. M., Wang, B.-C., and Kuhn, D. C. S., 2012. "Numerical study of pulsatile channel flows undergoing transition triggered by a modelled stenosis". *Phys. Fluids,* **24**(12), p. 121901.

[22] Beratlis, N., Balaras, E., and Kiger, K., 2009. "Direct numerical simulations of transitional pulsatile flow through a constriction". *J. Fluid Mech.,* **587**, pp. 425–451.

[23] Mittal, R., Simmons, S. P., and Najjar, F., 2003. "Numerical study of pulsatile flow in a constricted channel". *J. Fluid Mech.,* **485**, pp. 337–378.

[24] Beratlis, N., Balaras, E., Parvinian, B., and Kiger, K., 2005. "A numerical and experimental investigation of transitional pulsatile flow in a stenosed channel". *J. Biomech. Eng.,* **127**(7), pp. 1147–1157.

[25] Varghese, S. S., Frankel, S. H., and Fisher, P. F., 2007. "Direct numerical simulation of stenotic flows. Part 1. Steady flow". *J. Fluid Mech.,* **582**, pp. 253–280.

[26] Varghese, S. S., Frankel, S. H., and Fisher, P. F., 2007. "Direct numerical simulation of stenotic flows. Part 2. Pulsatile flow". *J. Fluid Mech.,* **582**, pp. 281–318.

[27] Varghese, S. S., Frankel, S. H., and Fischer, P. F., 2008. "Modeling transition to turbulence in eccentric stenotic flows". *J. Biomech. Eng.,* **130**(1), pp. 014503–014503–7.

[28] Tan, F. P. P., Wood, N. B., Tabor, G., and Xu, X. Y., 2011. "Comparison of LES of steady transitional flow in an idealized stenosed axisymmetric artery model with a RANS transitional model". *J. Biomech. Eng.,* **133**(5), pp. 051001–051001–12.

[29] Banks, J., and Bressloff, N. W., 2006. "Turbulence modeling in three-dimensional stenosed arterial bifurcations". *J. Biomech. Eng.,* **129**(1), pp. 40–50.

[30] Ghalichi, F., and Deng, X., 2003. "Turbulence detection in a stenosed artery bifurcation by numerical simulation of pulsatile blood flow using the low-Reynolds number turbulence model". *Biorheology,* **40**(6), pp. 637–654.

[31] Kaazempur-Mofrad, M., Isasi, A. G., Younis, H. F., Chan, R. C., Hinton, D. P., Sukhova, G., LaMuraglia, G. M., Lee, R. T., and Kamm, R. D., 2004. "Character-

ization of the atherosclerotic carotid bifurcation using MRI, finite element modeling, and histology". *Ann. Biomed. Eng.,* **32**(7), pp. 932–946.

[32] Schirmer, C. M., and Malek, A. M., 2011. "Computational fluid dynamic characterization of carotid bifurcation stenosis in patient-based geometries". *Brain and Behavior,* **2**(1), pp. 42–52.

[33] Stroud, J. S., Berger, S. A., and Saloner, D., 2001. "Numerical analysis of flow through a severely stenotic carotid artery bifurcation". *J. Biomech. Eng.,* **124**(1), pp. 9–20.

[34] Tan, F. P., Soloperto, G., Bashford, S., Wood, N. B., Thom, S., Hughes, A., and Xu, X. Y., 2008. "Analysis of flow disturbance in a stenosed carotid artery bifurcation using two-equation transitional and turbulence models". *J. Biomech. Eng.,* **130**(6), pp. 061008–061008–12.

[35] Dong, J., Inthavong, K., and Tu, J., 2013. "Image-based computational hemodynamics evaluation of atherosclerotic carotid bifurcation models". *Comput. Biol. Med.,* **43**(10), pp. 1353–1362.

[36] Rayz, V. L., Berger, S. A., and Saloner, D., 2007. "Transitional flows in arterial fluid dynamics". *Comput. Meth. Appl. Mech. Eng.,* **196**(31), pp. 3043–3048.

[37] Lee, S. E., Lee, S.-W., Fischer, P. F., Bassiouny, H. S., and Loth, F., 2008. "Direct numerical simulation of transitional flow in a stenosed carotid bifurcation". *J. Biomech.,* **41**(11), pp. 2551–2561.

[38] Kikinis, R., Pieper, S. D., and Vosburgh, K. G., 2014. *3D Slicer: A Platform for Subject-Specific Image Analysis, Visualization, and Clinical Support.* Springer New York, pp. 277–289.

[39] Ballyk, P. D., Steinman, D. A., and Ethier, C. R., 1994. "Simulation of non-newtonian blood flow in an end-to-side anastomosis". *Biorheology,* **31**(5), pp. 565–586.

[40] Sharp, M. K., Thurston, G. B., and Jr., J. E. M., 1996. "The effect of blood viscoelasticity on pulsatile flow in stationary and axially moving tubes". *Biorheology,* **33**(3), pp. 185–208.

[41] Gijsen, F. J., van de Vosse, F. N., and Janssen, J. D., 1999. "The influence of the non-newtonian properties of blood on the flow in large arteries: steady flow in a carotid bifurcation model". *J. Biomech.,* **32**(6), pp. 601–608.

[42] Ambrosi, D., Quarteroni, A., and Rozza, G., 2012. *Modeling of physiological flows.* Springer.

[43] Lee, S.-W., and Steinman, D. A., 2006. "On the relative importance of rheology for image-based CFD models of the carotid bifurcation". *J. Biomech. Eng.,* **129**(2), pp. 273–278.

[44] Thomas, J. B., Milner, J. S., Rutt, B. K., and Steinman, D. A., 2003. "Reproducibility of image-based computational fluid dynamics models of the human carotid bifurcation". *Ann. Biomed. Eng.,* **31**(2), pp. 132–141.

[45] Womersley, J. R., 1955. "Method for the calculation of velocity, rate of flow and viscous drag in arteries when the pressure gradient is known". *J. Physiol.,* **127**(3), pp. 553–563.

[46] Komen, E., Shams, A., Camilo, L., and Koren, B., 2014. "Quasi-DNS capabilities of openFOAM for different mesh types". *Comput. Fluid,* **96**, pp. 87 – 104.

[47] Eckhardt, B., Schneider, T., Hof, B., and Westerweel, J., 2007. "Turbulence transition in pipe flow". *Annu. Rev. Fluid Mech.,* **39**, pp. 447–468.

[48] Orlandi, P., and Fatica, M., 1997. "Direct simulations of turbulent flow in a pipe rotating about its axis". *J. Fluid Mech.,* **343**, p. 43–72.

[49] Quadrio, M., and Sibilla, S., 2000. "Numerical simulation of turbulent flow in a pipe oscillating around its axis". *J. Fluid Mech.,* **424**, p. 217–241.

[50] Smagorinsky, J., 1963. "General circulation experiments with the primitive equations". *Mon. Weather Rev.,* **91**(3), pp. 99–164.

[51] Launder, B. E., and Sharma, B. I., 1974. "Application of the energy-dissipation model of turbulence to the calculation of flow near a spinning disc". *Lett. Heat Mass Tran.,* **1**(2), pp. 131 – 137.

[52] Jones, W. P., and Launder, B. E., 1972. "The prediction of laminarization with a two-equation model of turbulence". *Int. J. Heat and Mass Transfer,* **15**(2), pp. 301 – 314.

[53] Wilcox, D. C., 1988. "Reassessment of the scale-determining equation for advanced turbulence models". *AIAA J.,* **26**(11), pp. 1299–1310.

[54] Walters, D. K., and Cokljat, D., 2008. "A three-equation eddy-viscosity model for Reynolds-averaged Navier-Stokes simulations of transitional flow". *J. Fluids Eng.,* **130**(12), pp. 121401–121401–14.

[55] Walters, D. K., and Leylek, J. H., 2004. "A new model for boundary layer transition using a single-point RANS approach". *J. Turbomach.,* **126**(1), pp. 193–202.

[56] Jacobs, R. G., and Durbin, P. A., 2001. "Simulations of bypass transition". *J. Fluid Mech.,* **428**, p. 185–212.

[57] Loeve, M., 1977. *Probability theory.* Springer.

[58] O'Donnell, T. F., 1986. "Pulsatile flow and atherosclerosis in the human carotid bifurcation: positive correlation between plaque location and low and oscillating shear stress". *J. Vasc. Surg.,* **3**(6), p. 944.

[59] He, X., and Ku, D. N., 1996. "Pulsatile flow in the human left coronary artery bifurcation: average conditions". *J. Biomech. Eng.,* **118**(1), pp. 74–82.

[60] Basavaraja, P., Surendran, A., Gupta, A., Saba, L., Laird, J. R., Nicolaides, A., Mtui, E. E., Baradaran, H., Lavra, F., and Suri, J. S., 2017. "Wall shear stress and oscillatory shear index distribution in carotid artery with varying degree of stenosis: a hemodinamic study". *J. Mech. Med. Biol.,* **17**(02), p. 1750037.

[61] Jeong, J., and Hussain, F., 1995. "On the identification of a vortex". *J. Fluid Mech.,* **285**, p. 69–94.

[62] Chakraborty, P., Balachandar, S., and Adrian, R. J., 2005. "On the relationships between local vortex identification schemes". *J. Fluid Mech.,* **535**, p. 189–214.

[63] Lopez, M., and Walters, D. K., 2016. "Prediction of transitional and fully turbulent flow using an alternative to the laminar kinetic energy approach". *J. Turbulence,* **17**(3), pp. 253–273.